













Variable-Temperature Plasmonic High-Entropy Carbides

Simon Divilov ^{1,2} Sean D. Griesemer ^{1,2} Robert C. Koennecker ^{3,4} Michael J. Ammendola ^{3,4}
Adam C. Zettel ^{1,2} Hagen Eckert ^{1,2} Jeffrey R. Shallenberger ⁵ Xiomara Campilongo ²
William G. Fahrenholtz ⁶ Arrigo Calzolari ^{7,1,2,*} Douglas E. Wolfe ^{4,†} and Stefano Curtarolo ^{1,2,‡}

¹Department of Mechanical Engineering and Materials Science, Duke University, Durham, NC 27708, USA

²Center for Extreme Materials, Duke University, Durham, NC 27708, USA

³Applied Research Laboratory, The Pennsylvania State University, University Park, PA 16802, USA

⁴Department of Materials Science and Engineering, The Pennsylvania State University, University Park, PA 16802, USA

⁵Materials Research Institute, The Pennsylvania State University, University Park, PA 16802, USA

⁶Department of Materials Science and Engineering, Missouri University of Science & Technology, Rolla, MO 65409, USA

⁷CNR-NANO Istituto Nanoscienze, Centro S3, I41125 Modena, Italy

Effective thermal management at variable and extreme temperatures face limitations for the development of novel energy and aerospace applications. Plasmonic approaches, shown to be capable of tailoring black-body emission, could be effective if materials with high-temperature and tunable plasmonic-resonance were available. Here, we report a synergy between experimental and theoretical results proving that many high-entropy transition-metal carbides, consisting of four or more metals at equal molar ratio, have plasmonic resonance at room, high ($>1000^\circ\text{C}$) and variable temperatures. We also found that these high-entropy carbides can be tuned and show considerable plasmonic thermal cycling stability. This paradigm-shift approach could prove quite advantageous as it facilitates the accelerated rational discovery and manufacturability of optically highly-optimized high-entropy carbides with ad-hoc properties.

Introduction

Thermal management — a challenge for efficiency and endurance of systems subjected to temperature variations [1, 2] — is crucial for extreme applications ($T > 1000^\circ\text{C}$). For example, understanding heat dissipation at high temperature (HT) [3] and under intense electromagnetic and radiation fields [4–10] is key for the development of critical technologies, necessary for nuclear fusion reactors [11] or aerospace applications [12].

In extreme environments, efforts to understand — both theoretically and experimentally — the physical mechanisms of heat/electrical conductivity, chemical degradation and optical response are limited in scope [13, 14]. In fact, existing attempts to address thermal management at HT, based on control of thermal conductivity demonstrate several limitations related to material endurance, structural integrity, and heat transport [15]. At extreme temperatures, thermal energy not only moves by lattice vibrations and charge carriers, but it is also emitted through the infrared part of the black-body radiation. Therefore, spectrum manipulation [16] has opened a new avenue for thermal management. For example, hyperbolic metamaterials have been proposed to overcome the Planck black-body thermal-emission limit [17–19] (so called super-Planckian [20]), and Sm-doping has been used to change emissivity of ZrB_2/SiC coatings for hypersonic flight.

Analogously, plasmonics would be promising since they are able to confine electromagnetic radiation to nanometer length-scales [21, 22] and to amplify local electric

fields [23]. For instance, plasmonic emitters [24] provide tunable narrow band radiation, even narrower than the black-body radiation at the same temperature. Unfortunately, resonance tunability to manipulate different parts of the spectra is possible only at low temperature (e.g. by alloying Au and Ag). Thus, the unavailability of high temperature tunable plasmonic systems mandates novel materials that would *simultaneously* require: **i.** high structural resistance to deformations at HT; **ii.** plasmonic activity in the near-IR/visible range under variable thermal conditions, where temperature may often change with large swings, **iii.** tunability, i.e. having a variety of resonance energies that can be modified by alloying; and **iv.** resistance to temperature cycles, i.e. restoring their initial plasmonic properties when the heating/cooling process is reversed.

Recently, in 2022, Calzolari et al. [25] theoretically proposed that multifunctional plasmonic high-entropy carbides (PHECs), a subset of the high-entropy carbide (HEC) realm [26, 27], could combine superior thermal and mechanical stability with plasmon activity in the near-IR and visible range at RT. With respect to binary refractory ceramics (e.g. TiN, ZrN, TaC) — which also stand out for their high melting points ($>3000^\circ\text{C}$), impressive mechanical hardness [28–32], and plasmonic response in the visible light range at HT [33–35] — the diverse composition of PHECs would also enable tuning of critical properties, such as the plasmon resonance energy [32].

In this article, we report a suite of experiments and calculations on PHECs demonstrating: **i.** plasmon resonance in the near-IR and visible light ranges at RT; **ii.** plasmonic character at HT of at least 1000°C , with only minor changes with respect to the RT; and **iii.** possibility to restore the initial plasmonic properties upon multiple thermal cycling from RT to HT. We chose a set of transition-metal PHECs by considering candidates with the highest likelihood of solid-solution functional synthe-

* arrigo.calzolari@nano.cnr.it

† dew125@psu.edu

‡ stefano@duke.edu

sizability [36], theoretical plasmonic intensity [25] and structural stability [37, 38]. PHEC ceramics were prepared by ball-milling mixtures of carbide precursors, followed by field-assisted sintering technology (FAST) high-temperature sintering [39]. Plasmonic properties were characterized by ellipsometry [40] from RT to 1000 °C. Reflective EELS (REELS) [41] and TEM-EELS [42] were further used to confirm the optical results. The experimental results were finally interpreted and analyzed through simulations from first-principles with density functional theory (DFT) that exploits the partial occupation (POCC) disorder method [43] to evaluate the optical properties of PHECs.

Here we identify a class of variable-temperature plasmonic HECs that simultaneously satisfy the need for chemically tunable and structurally stable plasmonic materials that maintain an unaltered optical response over a wide temperature range (300–1000 °C), and possibly beyond. Their high resistance to optical degradation upon extreme thermal treatments opens the way to unprecedented *variable temperature* plasmonic applications and impact manufacturability. The combination of disorder thermodynamic modeling, first-principle calculations, systematic growth, and characterization of new PHECs with customized optical properties, shows the benefit of our integrated approach.

Results

Sample selection and synthesis

We report new experimental results proving the existence of plasmon resonance in eleven HECs; the complete list and the compositions are summarized in Table I. A numerical label (1–11) is assigned to each system to simplify the notation. System 1 is the only 5-species carbide containing four transition metals (TMs) plus carbon. The remaining systems are 6-species HECs with five TMs. Systems 1–3 differ by a single species, and system 7 is the only one not including Ta.

Individual carbide powder precursors HfC, NbC, TaC, TiC, VC, WC, ZrC, and graphite were blended together in mixtures according to the targeted candidate compositions. FAST sintering was used to densify the blended and dry milled powders. More details about the synthesis of the compounds is discussed in the Methods Section. All HECs formed single-phase FCC crystals at a soak temperature and time of at least 2100 °C and 30 minutes, respectively; systems 6–8 and 11 required a higher temperature of 2300 °C and a longer soak time of 60 minutes to reach miscibility. The crystalline quality of the synthesized samples is demonstrated by the X-ray diffraction spectra reported in Supplementary Figure 1, where only small HfO₂-type oxide impurity peaks can be seen. Subsequent analysis of the raw starting powder indicated that the oxide inclusions were the result of higher-than-expected oxide concentration in the precursors. This was confirmed by scanning electron microscopy (SEM) images

of the polished cross sections of HECs (Supplementary Figure 2) which show the presence of oxide inclusions resulting from the impurities in the HfC precursor. Fortunately, HfO₂ impurities are transparent dielectrics that are not expected to have plasmon response in the near-IR/visible range, nor to affect the optical results of HEC compounds.

Ten of the eleven compositions had been synthesized as FCC single crystals before [25, 37, 44–48], whereas 3-HfNbTaWZrC₅ had not been previously synthesized. All HECs were computationally predicted to form single-phase FCC, based on the use of the disordered enthalpy-entropy descriptor (DEED) [36]. The successful synthesis of previously unrealized compound 3 provides additional validation of the DEED method. Details on sample preparation, experimental setups, and simulations can be found in the Methods Section.

Plasmonic resonance at room temperature

The optical properties of PHECs were measured by multi-technique spectroscopies. Specifically, we used ellipsometry to measure the real and imaginary parts of the energy (E)-dependent complex dielectric function $\hat{\epsilon}(\mathbf{q}, E) = \epsilon_r(\mathbf{q}, E) + i\epsilon_i(\mathbf{q}, E)$, as well as the electron energy loss spectrum $EELS(\mathbf{q}, E) = -\text{Im}[\hat{\epsilon}^{-1}(\mathbf{q}, E)]$, in the optical limit of zero transferred momentum ($\mathbf{q} = \mathbf{0}$) [49]. Plasmon excitations correspond to the poles of the complex dielectric function ($\hat{\epsilon} = 0$). As a consequence, the signature of a plasmon excitation is a peak in the EELS, at energy E_{peak} , where the height h_{peak} and full width at half maximum (FWHM) describe the intensity and the lifetime of the collective oscillations — i.e., sharp (diffuse) peaks indicate long (short) lived plasmon excitations. In this work, we focused on the low-energy part of the electromagnetic spectrum ($E < 5.0$ eV). Finally, first principles simulations of the POCC method have been carried out to compare and interpret the experimental results. All technical details on both experiments and simulations can be found in the Methods Section.

In order to prove the robustness and the accuracy of the ellipsometry results, REELS [41] and TEM-EELS [25, 42] techniques were also used to measure the $EELS(E)$ spectra of our HECs. Both ellipsometry and REELS are surface sensitive techniques: ellipsometry analyzes the change in polarization of reflected light, while REELS measures the energy loss of electrons reflected off the surface. In comparison to TEM-EELS, REELS has a much higher signal-to-noise ratio, allowing better determination of the peak position and distinguishing the characteristics of the plasmon peak with greater resolution. REELS has been used numerous times for plasmon detection in materials such as Si [50], SiC [51], and graphene [52]. Experimental details on REELS and TEM-EELS measurements are shown in Supplementary Figures 3 and 5.

As a first step, we measure the plasmonic response of the PHECs at RT. According to ellipsometry results (Figure 1), all PHECs exhibit a plasmon resonance in the range 1–3 eV; i.e., spanning the near-IR-visible portion of

	Composition	Ellipsometry								Simulation			
		E_0	E_0	E_{peak}	E_{peak}	FWHM	FWHM	h_{peak}	h_{peak}	E_0	E_{peak}	FWHM	h_{peak}
		RT	HT	RT	HT	RT	HT	RT	HT	[eV]	[eV]	[eV]	[a.u.]
		[eV]	[eV]	[eV]	[eV]	[eV]	[eV]	[a.u.]	[a.u.]	[eV]	[eV]	[eV]	[a.u.]
1	HfNbTaZrC ₄	1.53	1.25	1.81	1.75	1.12	1.30	0.089	0.068	1.75	1.80	0.78	0.094
2	HfNbTaTiZrC ₅	1.65	1.53	1.73	1.67	0.94	1.33	0.078	0.058	1.53	1.58	0.71	0.079
3	HfNbTaWZrC ₅	2.05	1.83	2.34	2.27	1.50	1.73	0.048	0.038	1.87	2.08	1.42	0.064
4	HfNbTaTiVC ₅	1.63	1.45	1.83	1.75	1.43	1.63	0.043	0.035	1.42	1.55	1.06	0.050
5	HfNbTaTiWC ₅	1.86	-	2.27	-	1.66	-	0.055	-	1.81	1.98	1.28	0.060
6	HfNbTaVZrC ₅	1.59	1.32	1.90	1.80	1.60	1.93	0.044	0.039	1.44	1.60	1.16	0.048
7	HfNbTiVZrC ₅	1.37	1.16	1.64	1.51	1.39	1.87	0.040	0.038	1.19	1.31	0.95	0.042
8	HfTaTiVZrC ₅	1.39	1.16	1.63	1.51	1.28	1.74	0.043	0.041	1.25	1.37	0.96	0.043
9	HfTaTiWZrC ₅	1.81	1.61	2.00	1.92	1.28	1.54	0.051	0.038	1.64	1.78	1.13	0.058
10	NbTaTiVWC ₅	2.17	2.04	2.29	2.20	2.08	1.99	0.027	0.020	1.75	1.84	1.05	0.043
11	NbTaTiVZrC ₅	1.73	1.56	1.90	1.81	1.48	1.73	0.042	0.036	1.37	1.50	1.04	0.049

TABLE I. **Properties from ellipsometry and calculations.** Optical properties of eleven PHEC compositions from ellipsometry experiments and DFT simulations at room (RT) and high temperatures (HT=1000 °C, a.u. = arbitrary unit).

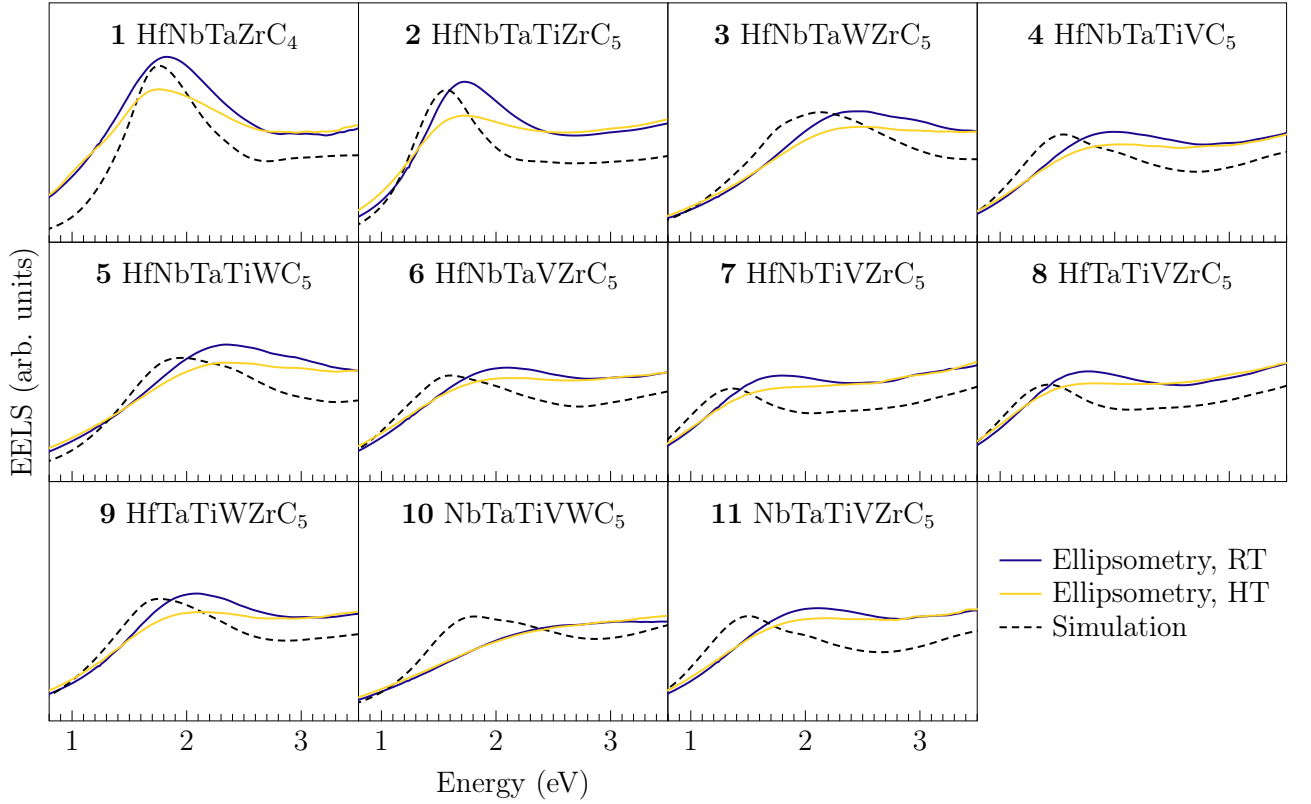


FIG. 1. **Ellipsometry versus simulations.** Room temperature (RT) and high temperature (HT) EELS spectra taken by ellipsometry, along with simulation results, for eleven HEC compositions (HT=1000 °C).

the electromagnetic spectrum, appealing for energy and telecommunication applications.

The agreement between ellipsometry (yellow line) and theoretical simulations (dashed black line) is very good, corroborating the REELS results (Supplementary Figure 4). Yet, ellipsometry and REELS results differ slightly: EELS peaks tend to be higher-energy, more intense, and wider than the respective REELS peaks. Such small but systematic spectral differences can be attributed to

spot size and volume of analysis, which can be affected by changes in composition and microstructure (Supplementary Figure 3). Simulation results, while remarkably in line with both experimental sets of data, tend to agree more closely with ellipsometry. More generally, the agreement between experiments and simulations is also remarkable as the simulations do not consider impurities, defects, or other microstructural features that may have effects on PHECs at room temperature. The excellent

agreement between experiments and simulations is an a posteriori confirmation of both the crystalline quality of the synthesized samples and the accuracy of the POCC method in modeling the optical properties of PHECs.

In order to investigate the plasmonic nature of the EELS peaks, we analyze the real (ϵ_r) and imaginary (ϵ_i) components of the dielectric function, resulting from the ellipsometry measurements and corresponding to the spectra of Figure 1. The data for PHECs are summarized in (Supplementary Figure 6).

The real part of the dielectric function is negative (metal-like) at energies of infrared and below, and crosses to positive (dielectric-like) in the near-IR and visible light ranges at the “crossover energy” E_0 , so that $\epsilon_r(E_0) \equiv 0$. At the same energy, the ϵ_i reaches a local minimum near zero. The condition $\hat{\epsilon} \simeq 0$ corresponds to the excitation of a so called “low-energy” or “screened” plasmon resonance, which involves the collective oscillation of a reduced fraction of the charge density, the rest being effectively screened by interband transitions (the smaller the magnitude ϵ_i , the longer the lifetime of the excitation). Full charge density oscillations (i.e., bulk plasmons) appear in EELS spectra as intense peaks in the ultraviolet region ($E > 20$ eV).

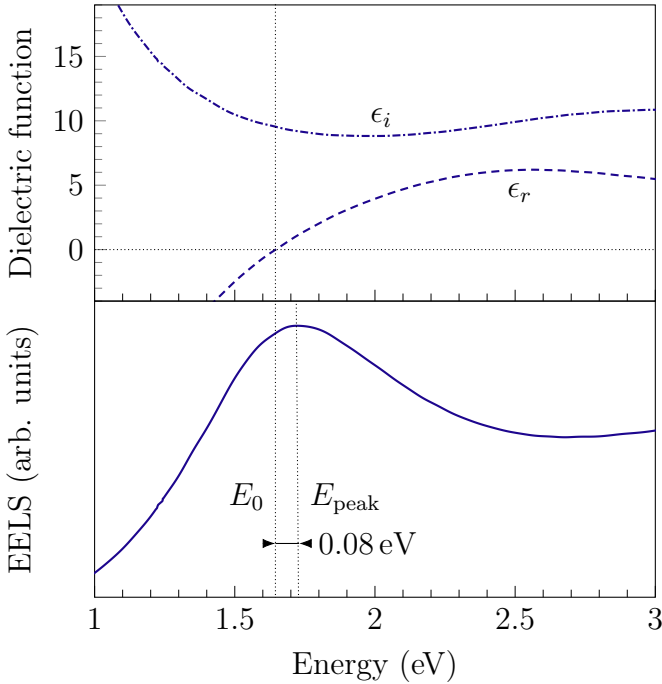


FIG. 2. **Peak versus crossover energy.** Dielectric function and EELS measured by ellipsometry at room temperature for 2-HfNbTaTiZrC₅.

Close inspection of both ellipsometry and simulated spectra indicates that the crossover energy E_0 is very close to the measured peak maximum energy E_{peak} , yet systematically smaller (within 0.2 eV). This is due to the non-ideal nature of the materials (i.e., dissipation, losses). This idea is illustrated in Figure 2. In an ideal

Drude electron gas, the whole complex dielectric function at crossover $\hat{\epsilon}(E_0)$ is zero, because of the lack of interband electronic dissipation leading to $\epsilon_i(E_0) = 0$, and therefore $\epsilon_r(E_0) \equiv 0$. This corresponds to a divergence in the EELS spectrum at $E_0 = E_{\text{peak}}$. In dissipative systems, the condition $\epsilon_i \neq 0$ removes the divergence, while the positive slope $d\epsilon_i/dE > 0$ for $E - E_0 \rightarrow 0^+$ is responsible for a positive contribution to the loss function that has a maximum at slightly higher energies, i.e., $E_0 \lesssim E_{\text{peak}}$. The smaller the losses, the closer E_0 and E_{peak} are, like in our cases. Therefore, we refer to E_{peak} as the plasmon energy of the system (see Supplementary Figure 7 for further details).

Resonance energies listed in Table I prove that HECs have tunable plasmonic properties with respect to composition — an advantage over other classes of plasmonic materials, such as noble metals and binary refractory ceramics. In Ref. 25, we discussed that the variation in E_{peak} between compositions is due to the balance among diverging effects induced by different transition metals. For instance, group-4 metals are responsible for red shifts of the plasmon energy, while group-6 metals cause a blue shift and broadening of the plasmon peak.

For analyzing plasmon’ lifetime, we fit the spectrum to a pseudo-Voigt function (combination of Gaussian and Lorentzian) with a linear background. The resonance peak heights h_{peak} and FWHM are tabulated in Table I. EELS intensities of the plasmonic peaks correlate to the density of states of TM d -orbitals [25, 53], crossing the Fermi energy, E_F (an example of the density of states for 1-HfNbTaZrC₄ is shown in Figure 3). In particular, the d -like conduction states (above E_F) are involved in optically active (i.e., dissipative) interband transitions from occupied p -orbitals of carbon $C(2p) \rightarrow \text{TM}(d)$ [30]. While the carbon contribution is similar in all PHECs, the energy distribution and the number of available empty d -states depend on the specific composition. Therefore, the stronger and more numerous interband transitions lead to higher ϵ_i ; as a consequence, the EELS peak is broader, and the lifetime of the plasmon excitation is shorter (i.e., lossy plasmons). The best 5-metal plasmonic candidate, having the highest h_{peak} and lowest FWHM within our set, is 2-HfNbTaTiZrC₅.

If we consider this composition in nanostructured materials for applications utilizing surface plasmons, the quality factor of the local plasmonic resonance Q [54] would be comparable to the best refractory carbide, TaC. All HECs quality factors are listed in Supplementary Table I. Notably, the parent binary rock-salt carbides (e.g., TiC, ZrC, HfC, VC) are generally not plasmonic, except TaC [25]. This indicates that the compositional disorder of HECs is beneficial for optical properties and it can be exploited for optimizing plasmonic response.

Plasmonic resonance at high temperature

To verify that the PHEC compositions remain plasmonic at HT, we heat the samples to 1000 °C at a rate of 30 °C/min, followed by 5 min of isothermal holding time, while performing the ellipsometry measurements. High

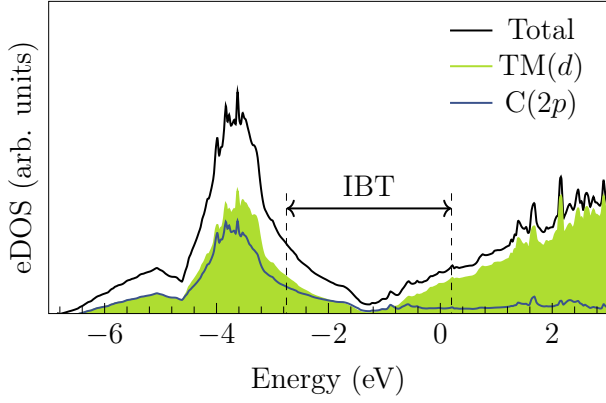


FIG. 3. **Electronic density of states.** Example of eDOS for 1-HfNbTaZrC₄, calculated for a single POCC tile. Zero energy reference is set to Fermi energy. Black line indicates the total eDOS, green area and blue line indicate the projected eDOS on transition metal (TM) *d* states, and carbon 2*p* orbitals, respectively. Black arrow pictorially represents an optically active interband transition (IBT) between occupied carbon 2*p* and empty transition metal (TM) *d* bands.

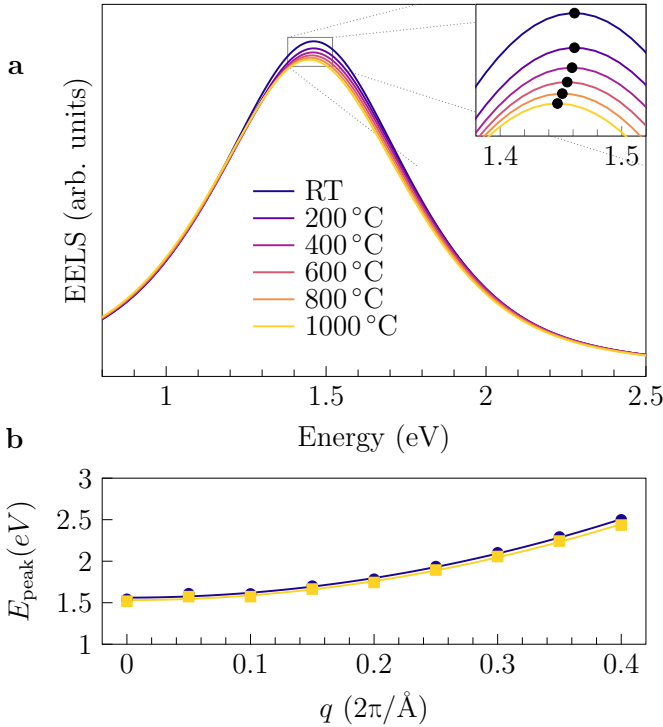


FIG. 4. **Simulated temperature dependence of the plasmonic properties of HfNbTaTiZrC₅.** **a** Simulated EELS at different temperatures. Inset shows the same spectra zoomed in at the peaks; the dots are the peak positions. The discrepancy between the spectra is mostly due to neglecting the electron-phonon interactions in the calculations, as described in the main text. **b** Simulated dispersion relation at room temperature (RT) and 1000 °C.

temperature EELS spectra are shown in Figure 1 (yellow lines), while the corresponding dielectric function plots are reported in Supplementary Figure 6.

The HT values of E_{peak} and E_0 are summarized in Table I. At HT, all of the PHEC samples maintain their plasmonic character. The spectra show that increasing temperature leads to only a slight red-shift ($\Delta E = 0.04$ – 0.2 eV) and weaker EELS intensity.

In order to confirm the thermal stability of the plasmonic response of PHECs, we additionally performed TEM-EELS measurements of 2-HfNbTaTiZrC₅ at RT and 1200 °C, plotted in Supplementary Figure 5a. They show peak energies of ~ 1.5 eV, very similar to the ones of simulation, ellipsometry, and REELS. While the TEM peak is resolvable, the data is much noisier, due to the very small beam size of ~ 1 nm² (comprising just a few unit cells), in contrast to the larger measurement regions of ellipsometry and REELS (~ 2500 μm^2). Therefore, when taken at different spots on the same sample, TEM-EELS produces variable peak parameters (Supplementary Figure 5b), whereas REELS measurements at different spots are highly uniform (Supplementary Figure 3a). Overall, the TEM-EELS results confirm that 2-HfNbTaTiZrC₅ is plasmonic of at least $T = 1200$ °C, enlarging the thermal stability range spanned by ellipsometry.

The analysis of complex dielectric spectra at HT (Supplementary Figure 6) indicates that the reduction and the broadening in EELS peak intensity observed in Figure 1 comes from a small decrease in the slope of ϵ_r and an increase in the local minimum value of ϵ_i at the energies near E_{peak} . This is an indication of a larger dissipative scattering rate, which includes several electronic processes [55]. For instance, the loss function can be expressed as $-\text{Im}[\epsilon^{-1}(E_{\text{peak}})] \approx E_{\text{peak}}/\gamma$, where γ is the electron scattering rate, which includes the effects of thermal atomic displacement on the band structures, and Fermi-Dirac broadening on the density of states around the Fermi level. Electron-phonon interactions [56] further contribute to the changes of the EELS peak. They are described by non-Hermitian self-energy operators [55], whose real part contributes to the red-shift of the plasmon energy, while the imaginary part increases the decoherence of the electron density oscillations (i.e., faster plasmon de-excitation) and reduces the EELS peak intensity [57].

Lattice thermal expansion [58], which reduces the effective free electron density, also contributes to the red-shift of E_{peak} with increasing temperature. This manifests as an increase in ϵ_r , such that the energy crossing (i.e., the plasmon energy) occurs at smaller values [34]. This result is also supported by first principles calculations in the temperature range 300–1000 °C. In this case, the temperature is the configurational temperature used to average the POCC ensemble, and the calculations include the effect of thermal expansion [46]. The resulting spectra (Figure 4a) agree qualitatively with our experiments (Figure 1), reproducing the bathochromic shift of the plasmonic peaks with increasing temperature. The

decrease in the EELS intensity is less severe in theoretical spectra than in experiments, because of lack of electron dissipative scattering effects in simulations that are known to increase with temperature [59].

While the identification of the single scattering contributions at HT is challenging, we indirectly investigated their effect on the plasmon lifetime by analyzing the FWHM modifications in the ellipsometry spectra; the results are summarized in Table I. We observe that the ranking of compositions by EELS intensities is almost the same at both RT and HT with a Pearson correlation coefficient of 0.97. While $\mathbf{2}\text{-HfNbTaTiZrC}_5$ is still the best material in our set, its Q value is not very high (see Supplementary Table 1), yet still good enough to support surface plasmon devices, especially in view of the existing Q -enhancement techniques [60].

Quadratic dispersion relations (E_0 versus transferred momentum \mathbf{q}) represent additional signatures of plasmonic excitations [32]. Plasmon dispersions of our PHECs were calculated with DFT. Given the computational cost of the entire POCC ensemble, we limited it to the most probable POCC tile (probability is the Boltzmann factor times the degeneracy; i.e., the cardinality of the factor group). The results for RT are found to be quadratic and are shown in Figure 5. For our best plasmonic candidate $\mathbf{2}\text{-HfNbTaTiZrC}_5$, we extend this analysis to the HT regime ($T = 1000^\circ\text{C}$), also including the lattice expansion effect. The results are shown in Figure 4b. The corresponding $E(\mathbf{q})$ curves still obey quadratic behavior, as in the RT case. These results confirm that the observed EELS peaks in HECs between RT and HT are a result of a plasmonic excitation.

Plasmonic resonance at variable temperatures

We tested the stability of the plasmonic resonance as a function of the temperature for system **2**: three heating/cooling cycles ($\text{RT} \rightleftharpoons \text{HT}$) are performed while optical properties are measured by ellipsometry. The results are shown in Figure 6 (a magnification around the EELS peak is shown in Supplementary Figure 8). The characteristics of the EELS, as a function of the cycling, remain unchanged in the vicinity of the plasmon resonance, in sharp contrast to other plasmonic materials [61]. In particular: **i.** during every single heating/cooling process, the EELS features change smoothly, without abrupt discontinuities; and **ii.** the changes in plasmonic properties induced by heating return to the RT state, indicating that the plasmonic properties of PHECs are reversible with temperature over several cycles. The reason lies in the phase stability of rock salt metal carbides. These compounds, and their binary precursors, are often sub-stoichiometric with *congruent melting* at few percent carbon-deficient from equicomposition. Their considerable range of solubility in the carbon-deficient region is bounded near equicomposition by a quite vertical rock salt \leftrightarrow graphite *solvus* [62]. Despite HECs phase diagrams are not as well characterized as their binary and ternary carbide precursors, they are expected to follow the same high temperature trends [36]. This is quite advantageous:

given a working temperature requirement and by playing with carbon composition, it is possible to synthesize HECs immune from graphitic segregation during heat cycles (graphite is not plasmonically active in our range of interest [63]), thus offering complete reversibility of the compound. Furthermore, low amount of oxygen impurities would not affect the plasmonic response as they would form transition metal oxycarbides with very low oxygen content at the invariant point [36]. In addition, carbon vacancies are not expected to disturb plasmonic resonance, which is dominated by the d -orbitals of the transition metals. The main effect of vacancies would be a change on the lifetime of the excitation given the inter-band transition of the carbon p -orbital electrons and TM d -orbitals [30] (Figure 4a of Ref. 25 and Figure 3). While our testing temperatures are already much higher than the usual for optical applications, we expect plasmonic resonance to be preserved at even higher temperatures $1000\text{-}2000^\circ\text{C}$, which are well below the melting temperature of HECs [64].

This implies that, at least for temperatures considered in this work, PHEC samples remain almost structurally unchanged; i.e., they do not undergo deformations that could affect bonding distribution/character and the overall free electronic charge density (responsible for the resonance). The increased thermal vibrations cause the observed decrease and shift of plasmonic peak in the EELS spectra through electron-phonon interactions. Such thermal stability is a special feature of PHECs over conventional plasmonic materials such as noble metals, which have lower melting points and would be irreversibly damaged at such temperatures.

Discussion

In this article, we have experimentally verified that, depending on the composition, HECs may have a plasmonic resonance both at RT and HT. We call this subset of carbides as PHECs. We have also shown that such resonance is tunable with composition, and extremely stable under variable temperature conditions. We found that excellent plasmonic stability and thermal cycling reversibility is achieved by designing the PHECs with carbon composition inside the sub stoichiometric solubility range. Furthermore, the plasmonic resilience to oxygen impurities is ascribed to the existence of the oxycarbide invariant point at low oxygen concentration.

In summary, four remarkable facts arise from this work: **i.** the initial screening for good plasmonic PHECs can be done at RT, avoiding HT measurements that are cumbersome and expensive; **ii.** even though dissipative processes contribute to EELS at HT, they are not strong enough to dominate the plasmon resonance; **iii.** PHECs that exhibit plasmonic response at HT, maintain the same optical properties over the entire temperature range; and **iv.** these PHECs show considerable plasmonic thermal cycling stability.

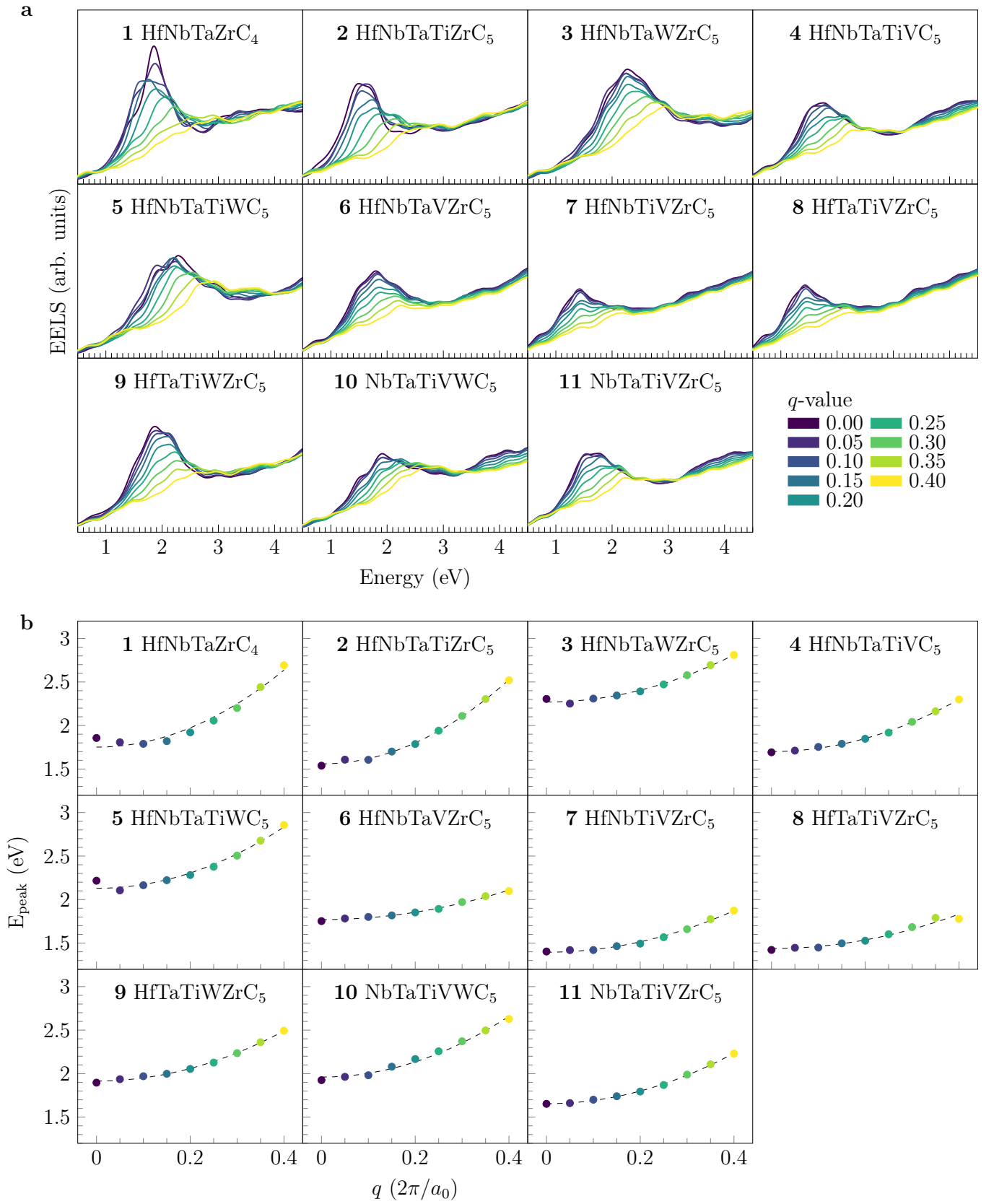


FIG. 5. **EELS spectra.** **a** Simulated EELS for different values of q (in units of $2\pi/a_0$ where a_0 is the lattice constant) for eleven HEC compositions. **b** Simulated dispersion $E_{\text{peak}}(q)$ for eleven HEC compositions. The dashed lines are a guide for the eyes.

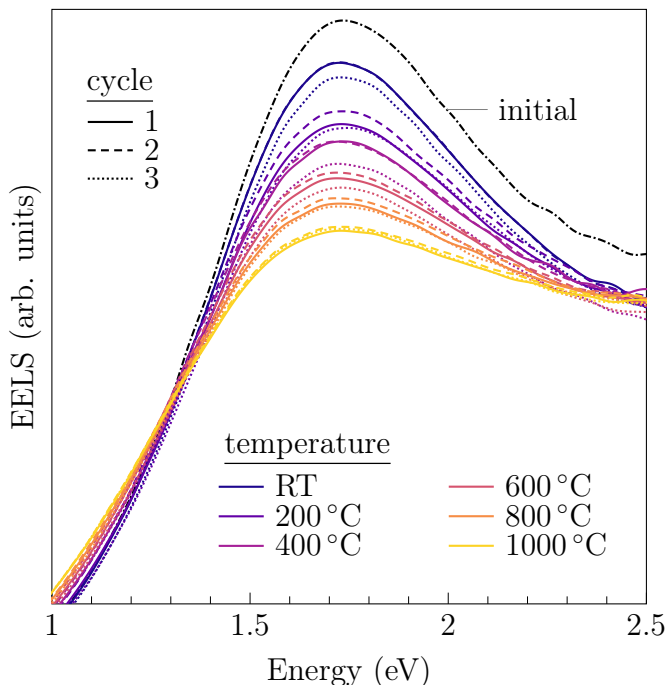


FIG. 6. **Temperature dependence of the plasmonic properties of HfNbTaTiZrC_5 .** EELS measured by ellipsometry over three heating-cooling cycles (#1, #2, and #3). Only spectra in the vicinity of the plasmonic resonance ($E_{\text{peak}} \approx 1.7 \text{ eV}$) are shown.

Our findings reveal a new class of variable-temperature plasmonic high-entropy carbide materials. In particular, their optical properties, coupled with their well-known mechanical stability, make them potential promising prototypes for manufacturing thermal plasmonic technologies at variable temperatures.

Methods

Synthesis

For the synthesis of HEC pellets, individual carbide powder precursors were blended together in mixtures according to the targeted candidate compositions. Starting powders consisted of HfC (99.0%, H.C. Starck), NbC (99.5%, Inframat Advanced Materials), TaC (99.5%, Stanford Advanced Materials), TiC (99.7%, Inframat Advanced Materials), VC (99.5%, SkySpring Nanomaterials), WC (99.9%, Inframat Advanced Materials), ZrC (99.9% purity, U.S. Research Nanomaterials), and graphite (99.0%, Asbury Graphite Mills). Batches were mixed by dry milling for 24 hours at 200 rpm in a 125 mL high-density polyethylene bottle; milling was performed in a 1:11 mass ratio of powder to 10 mm yttria-stabilized zirconia (YSZ) media. FAST was used to densify the blended powders into 20 mm bulk samples. Sintering was carried out under $\sim 3 \text{ mTorr}$ vacuum in a 25 Ton FAST system (FCT Systeme GmbH), with soak temperatures

ranging between 2100 and 2300 °C, soak times between 30 and 60 min, and a ramped loading segment in which the applied pressure increased from 30 to 50 MPa during the heating sequence (100 °C/min). More details regarding this FAST system setup for material processing can be found in our previous reference [36].

Ellipsometry

To measure temperature-dependent spectroscopic ellipsometry, HEC samples were polished to mirror finish and cleaned sequentially with acetone, ethanol, and deionized water. Samples were then mounted individually on a sample holder using spot-welded tantalum strips. After cleaning and mounting, samples were loaded into the load lock of a molecular beam epitaxy (MBE) system and, after reaching a base pressure lower than $1 \times 10^{-6} \text{ Torr}$, outgassed at 120 °C for 60 min. Upon finish outgassing and allowing the load lock to cool down overnight, samples were transferred into a model R450 MBE reactor from DCA Instruments at a background pressure lower than $5 \times 10^{-8} \text{ Torr}$. In the MBE reactor, *in-situ* temperature-dependent ellipsometry measurements were performed using an M-2000 *in-situ* ellipsometer model X-210 with near infrared upgrade from J.A. Woollam. Single spectra were recorded in the range from 210 to 1690 nm and acquired through the long spectrum acquisition mode in the J.A. Woollam CompleteEase software. Sample height and alignment were calibrated to maximize ellipsometry signal intensity. For each sample, an ellipsometry measurement was taken immediately after transfer into the MBE chamber at room temperature. All samples were then heated in sequence to 1000 °C and cooled to 800, 600, 400, and 200 °C using a ramp rate of 30 °C/min. After stabilizing at each of the target temperatures for 5 min, ellipsometry spectra were recorded at background pressures below $5 \times 10^{-8} \text{ Torr}$. A final ellipsometry spectrum was taken in analogy to the initial measurement at room temperature when the sample temperature reached 27 °C after the heating cycle. Temperatures were measured by a thermocouple mounted inside the MBE sample stage facing the backside of the sample.

Modeling the dielectric function

Disordered systems are simulated by using the POCC method, which considers the system as an ensemble average of ordered representative states — tiles [43]. For each tile j , DFT is used to compute the factor-group degeneracy g_j , enthalpy H_j , and complex dielectric function $\hat{\epsilon}_j(\mathbf{q}, E)$. Then, the complex dielectric function of the disordered system is given by:

$$\langle \hat{\epsilon}_j(\mathbf{q}, E; T) \rangle = \sum_j P_j(T) \hat{\epsilon}_j(\mathbf{q}, E) \quad (1)$$

where $P_j(T) = g_j e^{-H_j/k_B T} / \sum_j g_j e^{-H_j/k_B T}$ with T and k_B the experimental sintering temperature and the Boltzmann constant, respectively. Unless otherwise stated, $\hat{\epsilon}_j$ is calculated in the optical limit $\mathbf{q} = \mathbf{0}$, using the Green-Kubo formula with the VASP package, and random phase approximation (RPA) excluding local-field effects (LFE),

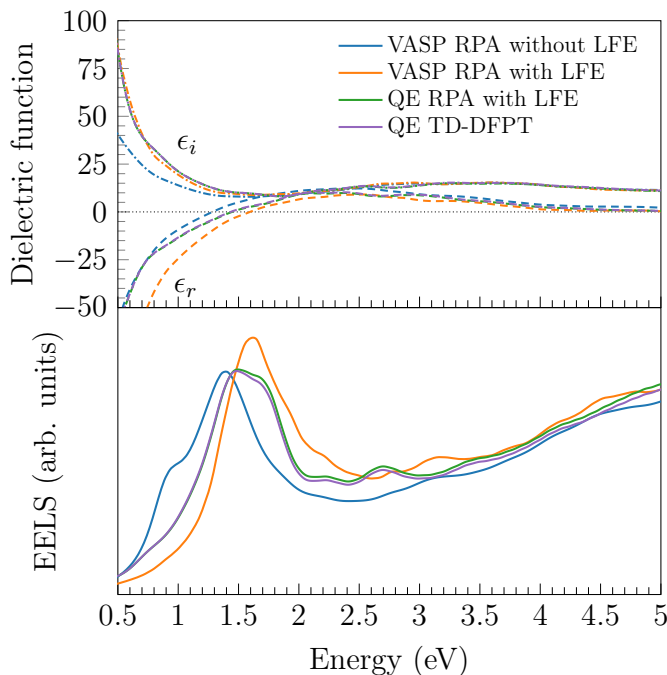


FIG. 7. **Comparison of ab-initio approximations.** Comparison of dielectric function and EELS using VASP with RPA with and without LFE, QE with RPA with LFE, and QE with time-dependent density functional perturbation theory (TD-DFPT) for a representative POCC tile of HfNbTaTiZrC_5 .

i.e., contributions due to the electron density inhomogeneity [65]. To handle the case when $\mathbf{q} \neq \mathbf{0}$, we use Quantum Espresso (QE) in the RPA including LFE [66]. All calculations are performed using the Perdew-Burke-Ernzerhof functional [67] with the convergence parameters set (energy cutoff, k-point sampling, etc.) by the AFLOW standard [68]. In Figure 7, we show the complex dielectric function and EELS spectra for a representative POCC tile of HfNbTaTiZrC_5 , calculated using the Drude-Lorentz model within the random phase approximation (RPA), as implemented in VASP and QE codes, with and without the local field effects (LFE). The results are also compared with spectra simulated by using the time-dependent density functional perturbation theory (TD-DFPT) approach implemented in the *turbo-eels* code, also included in the QE suite. In the latter case,

spectra are evaluated in the limit of vanishing transferred momentum ($\mathbf{q} \rightarrow \mathbf{0}$). The four set of spectra are in excellent agreement, within the numerical errors. The small deviation between the VASP and QE RPA results is attributed to local field effects (LFE), which can slightly shift the peak positions, especially at low energies [69].

Data availability

The code used to generate and process dielectric simulation data will be publicly available upon the release of the next version of AFLOW. Processed data used in this work are also available from the corresponding author upon reasonable request.

Acknowledgements

The authors thank Cormac Toher, Scott Thiel, Michael Mehl, and Lucas Wilson for fruitful discussions. The authors also thank Stephanie Law and Maria Hilse for providing assistance with the ellipsometry experiments. This research was supported by the Office of Naval Research under grants N00014-23-1-2615 and N00014-24-1-2768. This work was supported by high-performance computer time and resources from the DoD High Performance Computing Modernization Program (Frontier). We acknowledge Auro Scientific, LLC for computational support.

Contributions

Authors Simon Divilov, Sean Griesemer, and Robert Koennecker contributed equally to the project. S. C. and A. C. conceptualized the disorder expansion for dielectric properties. S. D. and S. D. G. performed the simulations and wrote the code to process simulation results. R. C. K. and M. J. A. synthesized the samples, performed experiments and contributed to writing the paper. A. C. Z. co-wrote the code to process simulation results. H. E., S. D. and S. C. wrote appropriate parts of the AFLOW code and advised on the simulations. J. R. S. advised on the REELS technique. X. C. contributed to paper writing. A. C., D. E. W., and S. C. established the research direction and supervised the project. All the authors contributed to the writing of the manuscript.

Conflict of interest

The authors declare no competing interests.

Supplementary information

The online version contains supplementary material available at...

- [1] Y. Shabany, *Heat Transfer: Thermal Management of Electronics* (CRC Press, 2009).
- [2] S. Jafari and T. Nikolaidis, *Thermal Management Systems for Civil Aircraft Engines: Review, Challenges and Exploring the Future*, Applied Sciences **8**, 2044 (2018), doi:10.3390/app8112044.
- [3] M. T. Keif and R. H. Victora, *Materials for Heat-Assisted Magnetic Recording*, MRS Bull. **43**, 87–92 (2018), doi:

10.1557/mrs.2018.2.

- [4] C. Wu, B. N. III, J. John, A. Milder, B. Zollars, S. Savoy, and G. Shvets, *Metamaterial-Based Integrated Plasmonic Absorber/Emitter for Solar Thermo-Photovoltaic Systems*, J. Opt. **14**, 024005 (2012), doi:10.1088/2040-8978/14/2/024005.
- [5] S. Pillai and M. A. Green, *Plasmonics for Photovoltaic Applications*, Sol. Energy Mater. Sol. Cells **94**, 1481–1486

- (2010), doi:10.1016/j.solmat.2010.02.046.
- [6] S. V. Boriskina, H. Ghasemi, and G. Chen, *Plasmonic Materials for Energy: From Physics to Applications*, Mater. Today **16**, 375–386 (2013), doi:10.1016/j.mattod.2013.09.003.
 - [7] J. Cunha, T. Guo, G. D. Valle, A. N. Koya, R. P. Zaccaria, and A. Alabastri, *Controlling Light, Heat, and Vibrations in Plasmonics and Phononics*, Adv. Opt. Mater. **8**, 2001225 (2020), doi:10.1002/adom.202001225.
 - [8] D. Zhao, Z. Lin, W. Zhu, H. J. Lezec, T. Xu, A. Agrawal, C. Zhang, and K. Huang, *Recent Advances in Ultraviolet Nanophotonics: From Plasmonics and Metamaterials to Metasurfaces*, Nanophotonics **10**, 2283–2308 (2021), doi:10.1515/nanoph-2021-0083.
 - [9] A. Ahmadvand, B. Gerislioglu, R. Ahuja, and Y. K. Mishra, *Terahertz Plasmonics: The Rise of Toroidal Metadevices Towards Immunobiosensings*, Mater. Today **32**, 108–130 (2020), doi:10.1016/j.mattod.2019.08.002.
 - [10] L. Jauffred, A. Samadi, H. Klingberg, P. M. Bendix, and L. B. Oddershede, *Plasmonic Heating of Nanostructures*, Chem. Rev. **119**, 8087–8130 (2019), doi:10.1021/acs.chemrev.8b00738.
 - [11] S. McSherry, M. Webb, J. Kaufman, Z. Deng, A. Davoodabadi, T. Ma, E. Kioupakis, K. Esfarjani, J. T. Heron, and A. Lenert, *Nanophotonic control of thermal emission under extreme temperatures in air*, Nat. Nanotechnol. **17**, 1104–1110 (2022), doi:10.1038/s41565-022-01205-1.
 - [12] A. B. Peters, D. Zhang, S. Chen, C. Ott, C. Oses, S. Curtarolo, I. McCue, T. Pollock, and S. E. Prameela, *Materials Design for Hypersonics*, Nat. Commun. **15**, 3328 (2024), doi:10.1038/s41467-024-46753-3.
 - [13] B. Esser, J. Barcena, M. Kuhn, A. Okan, L. Haynes, S. Gianella, A. Ortona, V. Liedtke, D. Francesconi, and H. Tanno, *Innovative Thermal Management Concepts and Material Solutions for Future Space Vehicles*, Journal of Spacecraft and Rockets **53**, 1051–1060 (2016), doi:10.2514/1.A33501.
 - [14] Y. Dong, E. Wang, Y. You, C. Yin, and Z. Wu, *Thermal Protection System and Thermal Management for Combined-Cycle Engine: Review and Prospects*, Energies **12**, 240 (2019), doi:10.3390/en12020240.
 - [15] Y.-G. Lv, Y.-T. Wang, T. Meng, Q.-W. Wang, and W.-X. Chu, *Review on thermal management technologies for electronics in spacecraft environment*, Energy Storage and Saving **3**, 153–189 (2024), doi:10.1016/j.enss.2024.03.001.
 - [16] J. C. Cuevas and F. J. García-Vidal, *Radiative Heat Transfer*, ACS Photonics **5**, 3896–3915 (2018), doi:10.1021/acsp Photonics.8b01031.
 - [17] J. Yang, W. Du, Y. Su, Y. Fu, S. Gong, S. He, and Y. Ma, *Observing of the super-Planckian near-field thermal radiation between graphene sheets*, Nat. Commun. **9**, 4033 (2018), doi:10.1038/s41467-018-06163-8.
 - [18] Y. Guo, C. L. Cortes, S. Molesky, and Z. Jacob, *Broadband super-Planckian thermal emission from hyperbolic metamaterials*, Appl. Phys. Lett. **101**, 131106 (2012), doi:10.1063/1.4754616.
 - [19] I. S. Nefedov and L. A. Melnikov, *Super-Planckian far-zone thermal emission from asymmetric hyperbolic metamaterials*, Appl. Phys. Lett. **105**, 161902 (2014), doi:10.1063/1.4899126.
 - [20] Y. Xiao, M. Sheldon, and M. A. Kats, *Super-Planckian emission cannot really be ‘thermal’*, Nature Photonics **16**, 397–401 (2022), doi:10.1038/s41566-022-01005-y.
 - [21] J. A. Schuller, E. S. Barnard, W. Cai, Y. C. Jun, J. S. White, and M. L. Brongersma, *Plasmonics for Extreme Light Concentration and Manipulation*, Nat. Mater. **9**, 193–204 (2010), doi:10.1038/nmat2630.
 - [22] M. S. Tame, K. R. McEnery, Ş. K. Özdemir, J. Lee, S. A. Maier, and M. S. Kim, *Quantum Plasmonics*, Nat. Phys. **9**, 329–340 (2013), doi:10.1038/nphys2615.
 - [23] P. Berini and I. D. Leon, *Surface Plasmon-Polariton Amplifiers and Lasers*, N. Photon. **6**, 16–24 (2012), doi:10.1038/nphoton.2011.285.
 - [24] D. Costantini, A. Lefebvre, A.-L. Coutrot, I. Moldovan-Doyen, J.-P. Hugonin, S. Boutami, F. Marquier, H. Benisty, and J.-J. Greffet, *Plasmonic Metasurface for Directional and Frequency-Selective Thermal Emission*, Phys. Rev. Applied **4**, 014023 (2015), doi:10.1103/PhysRevApplied.4.014023.
 - [25] A. Calzolari, C. Oses, C. Toher, M. Esters, X. Campilongo, S. P. Stepanoff, D. E. Wolfe, and S. Curtarolo, *Plasmonic high-entropy carbides*, Nat. Commun. **13**, 5993 (2022), doi:10.1038/s41467-022-33497-1.
 - [26] C. Oses, C. Toher, and S. Curtarolo, *High-entropy ceramics*, Nat. Rev. Mater. **5**, 295–309 (2020), doi:10.1038/s41578-019-0170-8.
 - [27] C. Toher, C. Oses, D. Hicks, and S. Curtarolo, *Unavoidable disorder and entropy in multi-component systems*, npj Comput. Mater. **5**, 69 (2019), doi:10.1038/s41524-019-0206-z.
 - [28] U. Guler, A. Boltasseva, and V. M. Shalaev, *Refractory Plasmonics*, Science **344**, 263–264 (2014), doi:10.1126/science.1252722.
 - [29] O. Cedillos-Barraza, D. Manara, K. Boboridis, T. Watkins, S. Grasso, D. D. Jayaseelan, R. J. M. Konings, M. J. Reece, and W. E. Lee, *Investigating the highest melting temperature materials: A laser melting study of the TaC-HfC system*, Sci. Rep. **6**, 37962 (2016), doi:10.1038/srep37962.
 - [30] M. Kumar, N. Umezawa, S. Ishii, and T. Nagao, *Examining the Performance of Refractory Conductive Ceramics as Plasmonic Materials: A Theoretical Approach*, ACS Photonics **3**, 43–50 (2016), doi:10.1021/acsp Photonics.5b00409.
 - [31] A. Catellani and A. Calzolari, *Plasmonic Properties of Refractory Titanium Nitride*, Phys. Rev. B **95**, 115145 (2017), doi:10.1103/PhysRevB.95.115145.
 - [32] A. Catellani, P. D’Amico, and A. Calzolari, *Tailoring the Plasmonic Properties of Metals: The Case of Substoichiometric Titanium Nitride*, Phys. Rev. Materials **4**, 015201 (2020), doi:10.1103/PhysRevMaterials.4.015201.
 - [33] S. T. Sundari, R. Ramaseshan, F. Jose, S. Dash, and A. K. Tyagi, *Investigation of Temperature Dependent Dielectric Constant of a Sputtered TiN Thin Film by Spectroscopic Ellipsometry*, J. Appl. Phys. **115** (2014), doi:10.1063/1.4862485.
 - [34] H. G. Reddy, U. Guler, Z. Kudyshev, A. V. Kildishev, V. M. Shalaev, and A. Boltasseva, *Temperature-Dependent Optical Properties of Plasmonic Titanium Nitride Thin Films*, ACS Photonics **4**, 1413–1420 (2017), doi:10.1021/acsp Photonics.7b00127.
 - [35] T. Krekeler, S. S. Rout, G. V. Krishnamurthy, M. Störmer, M. Arya, A. Ganguly, D. S. Sutherland, S. I. Bozhevolnyi, M. Ritter, K. Pederson, A. Y. Petrov, M. Eich, and M. Chirumamilla, *Unprecedented Thermal Stability of Plasmonic Titanium Nitride Films up*

- to 1400°C, *Adv. Opt. Mater.* **9**, 2100323 (2021), doi:10.1002/adom.202100323.
- [36] S. Divilov, H. Eckert, D. Hicks, C. Oses, C. Toher, R. Friedrich, M. Esters, M. J. Mehl, A. C. Zettl, Y. Lederer, E. Zurek, J.-P. Maria, D. W. Brenner, X. Campilongo, S. Filipovic, W. G. Fahrenholtz, C. J. Ryan, C. M. DeSalle, R. J. Creales, D. E. Wolfe, A. Calzolari, and S. Curtarolo, *Disordered enthalpy-entropy descriptor for high-entropy ceramics discovery*, *Nature* **625**, 66–73 (2024), doi:10.1038/s41586-023-06786-y.
- [37] P. Sarker, T. Harrington, C. Toher, C. Oses, M. Samiee, J.-P. Maria, D. W. Brenner, K. S. Vecchio, and S. Curtarolo, *High-entropy high-hardness metal carbides discovered by entropy descriptors*, *Nat. Commun.* **9**, 4980 (2018), doi:10.1038/s41467-018-07160-7.
- [38] T. J. Harrington, J. Gild, P. Sarker, C. Toher, C. M. Rost, O. F. Dippo, C. McElfresh, K. Kaufmann, E. Marin, L. Borowski, P. E. Hopkins, J. Luo, S. Curtarolo, D. W. Brenner, and K. S. Vecchio, *Phase stability and mechanical properties of novel high entropy transition metal carbides*, *Acta Mater.* **166**, 271–280 (2019), doi:10.1016/j.actamat.2018.12.054.
- [39] D. E. Wolfe, P. E. Albert, C. J. Ryan, J. A. Reiss, S. P. Stepanoff, and P. Kolonin, *Optimized processing of high density ternary hafnium-tantalum carbides via field assisted sintering technology for transition into hypersonic applications*, *J. Eur. Ceram. Soc.* **42**, 327–335 (2022), doi:10.1016/j.jeurceramsoc.2021.10.014.
- [40] H. Fujiwara, *Spectroscopic Ellipsometry: Principles and Applications* (John Wiley & Sons, 2007), doi:10.1002/9780470060193.
- [41] Z. L. Wang and J. M. Cowley, *Reflection electron energy loss spectroscopy (REELS): A technique for the study of surfaces*, *Surf. Sci.* **193**, 501–512 (1988), doi:10.1016/0039-6028(88)90449-9.
- [42] R. F. Egerton, *Electron energy-loss spectroscopy in the electron microscope* (Springer Science & Business Media, 2011), doi:10.1007/978-1-4419-9583-4.
- [43] K. Yang, C. Oses, and S. Curtarolo, *Modeling Off-Stoichiometry Materials with a High-Throughput Ab-Initio Approach*, *Chem. Mater.* **28**, 6484–6492 (2016), doi:10.1021/acs.chemmater.6b01449.
- [44] E. Castle, T. Csanádi, S. Grasso, J. Dusza, and M. Reece, *Processing and Properties of High-Entropy Ultra-High Temperature Carbides*, *Sci. Rep.* **8**, 8609 (2018), doi:10.1038/s41598-018-26827-1.
- [45] J. Zhou, J. Zhang, F. Zhang, B. Niu, L. Lei, and W. Wang, *High-entropy Carbide: A Novel Class of Multicomponent Ceramics*, *Ceram. Int.* **44**, 22014–22018 (2018), doi:10.1016/j.ceramint.2018.08.100.
- [46] X. Yan, L. Constantin, Y. Lu, J.-F. Silvain, M. Nastasi, and B. Cui, *(Hf_{0.2}Zr_{0.2}Ta_{0.2}Nb_{0.2}Ti_{0.2})C high-entropy ceramics with low thermal conductivity*, *J. Am. Ceram. Soc.* **101**, 4486–4491 (2018), doi:10.1111/jace.15779.
- [47] E. Chicardi, C. García-Garrido, and F. J. Gotor, *Low temperature synthesis of an equiatomic (TiZrHfVNb)C₅ high entropy carbide by a mechanically-induced carbon diffusion route*, *Ceram. Int.* **45**, 21858–21863 (2019), doi:10.1016/j.ceramint.2019.07.195.
- [48] E. Chicardi, C. García-Garrido, J. Hernández-Saz, and F. J. Gotor, *Synthesis of all equiatomic five-transition metals High Entropy Carbides of the IVB (Ti, Zr, Hf) and VB (V, Nb, Ta) groups by a low temperature route*, *Ceram. Int.* **46**, 21421–21430 (2020), doi:10.1016/j.ceramint.2020.05.240.
- [49] D. Pines, *Elementary Excitations In Solids*, *Frontiers in Physics* (Westview Press, 1999).
- [50] L. H. Yang, K. Tőkési, J. Tóth, B. Da, H. M. Li, and Z. J. Ding, *Optical Properties of Silicon and Germanium Determined By High-Precision Analysis of Reflection Electron Energy Loss Spectroscopy Spectra*, *Phys. Rev. B* **100**, 245209 (2019), doi:10.1103/PhysRevB.100.245209.
- [51] J. Costantini and J. Ribis, *Analysis of Plasmon Loss Peaks of Oxides and Semiconductors with the Energy Loss Function*, *Materials* **16**, 7610 (2023), doi:10.3390/ma16247610.
- [52] Y. Liu, R. F. Willis, K. V. Emtsev, and T. Seyller, *Plasmon Dispersion and Damping in Electrically Isolated Two-Dimensional Charge Sheets*, *Phys. Rev. B* **78**, 201403 (2008), doi:10.1103/PhysRevB.78.201403.
- [53] M. S. Dresselhaus, G. Dresselhaus, and A. Jorio, *Group Theory: Application to the Physics of Condensed Matter* (Springer, 2007).
- [54] F. Wang and Y. R. Shen, *General Properties of Local Plasmons in Metal Nanostructures*, *Phys. Rev. Lett.* **97**, 206806 (2006), doi:10.1103/physrevlett.97.206806.
- [55] S. Zollner, F. Abadizaman, C. Emminger, and N. Samarasingha, *Spectroscopic ellipsometry from 10 to 700 K*, *Adv. Opt. Tech.* **11**, 117–135 (2022), doi:10.1515/aot-2022-0016.
- [56] F. Wang and Y. R. Shen, *Electron-phonon interactions from first principles*, *Rev. Mod. Phys.* **89**, 015003 (2017), doi:10.1103/revmodphys.89.015003.
- [57] M. L. Cohen and S. G. Louie, *Fundamentals of Condensed Matter Physics* (Cambridge University Press, 2016), doi:10.1017/CBO9781139031783.
- [58] M. Baleva, T. Georgiev, and G. Lashkarev, *On the temperature dependence of the energy gap in PbSe and PbTe*, *J. Phys.: Condens. Matter* **2**, 2935–2940 (1990), doi:10.1088/0953-8984/2/13/003.
- [59] M. Kaveh and N. Wiser, *Electron-electron scattering in conducting materials*, *Adv. Phys.* **33**, 257–372 (1984), doi:10.1080/00018738400101671.
- [60] B. Tandon, S. Ghosh, and D. J. Milliron, *Dopant Selection Strategy for High-Quality Factor Localized Surface Plasmon Resonance from Doped Metal Oxide Nanocrystals*, *Chem. Mater.* **31**, 7752–7760 (2019), doi:10.1021/acs.chemmater.9b02917.
- [61] M. P. Wells, R. Bower, R. Kilmurray, B. Zou, A. P. Mi-hai, G. Gobalakrishnan, N. M. Alford, R. F. M. Oulton, L. F. Cohen, S. A. Maier, A. V. Zayats, and P. K. Petrov, *Temperature stability of thin film refractory plasmonic materials*, *Optics Express* **26**, 15726 (2018), doi:10.1364/oe.26.015726.
- [62] T. B. Massalski, H. Okamoto, P. R. Subramanian, and L. Kacprzak, eds., *Binary Alloy Phase Diagrams* (ASM International, Materials Park, Ohio, USA, 1990).
- [63] A. B. Djurišić and E. H. Li, *Optical properties of graphite*, *J. Appl. Phys.* **85**, 7404–7410 (1999), doi:10.1063/1.369370.
- [64] S. Liu, S. Zhang, S. Liu, D. Li, Y. Li, and S. Wang, *Phase stability, mechanical properties and melting points of high-entropy quaternary metal carbides from first-principles*, *J. Eur. Ceram. Soc.* **41**, 6267–6274 (2021), doi:10.1016/j.jeurceramsoc.2021.05.022.
- [65] M. Gajdoš, K. Hummer, G. Kresse, J. Furthmüller, and F. Bechstedt, *Linear optical properties in the projector-augmented wave methodology*, *Phys. Rev. B* **73**, 045112

- (2006), doi:10.1103/PhysRevB.73.045112.
- [66] P. Giannozzi, O. Andreussi, T. Brumme, O. Bunau, M. Buongiorno Nardelli, M. Calandra, R. Car, C. Cavazzoni, D. Ceresoli, M. Cococcioni, N. Colonna, I. Carnimeo, A. Dal Corso, S. de Gironcoli, P. Delugas, R. A. DiStasio Jr., A. Ferretti, A. Floris, G. Fratesi, G. Fugallo, R. Gebauer, U. Gerstmann, F. Giustino, T. Gorni, J. Jia, M. Kawamura, H.-Y. Ko, A. Kokalj, E. Küçükbenli, M. Lazzeri, M. Marsili, N. Marzari, F. Mauri, N. L. Nguyen, H.-V. Nguyen, A. Otero-de-la-Roza, L. Paulatto, S. Poncé, D. Rocca, R. Sabatini, B. Santra, M. Schlipf, A. P. Seitsonen, A. Smogunov, I. Timrov, T. Thonhauser, P. Umari, N. Vast, X. Wu, and S. Baroni, *Advanced capabilities for materials modelling with Quantum ESPRESSO*, J. Phys.: Condens. Matter **29**, 465901 (2017), doi:10.1088/1361-648X/aa8f79.
- [67] J. P. Perdew, K. Burke, and M. Ernzerhof, *Generalized Gradient Approximation Made Simple*, Phys. Rev. Lett. **77**, 3865–3868 (1996), doi:10.1103/PhysRevLett.77.3865.
- [68] C. Oses, M. Esters, D. Hicks, S. Divilov, H. Eckert, R. Friedrich, M. J. Mehl, A. Smolyanyuk, X. Campilongo, A. van de Walle, J. Schroers, A. G. Kusne, I. Takeuchi, E. Zurek, M. Buongiorno Nardelli, M. Fornari, Y. Lederer, O. Levy, C. Toher, and S. Curtarolo, *aflo++: A C++ framework for autonomous materials design*, Comput. Mater. Sci. **217**, 111889 (2023), doi:10.1016/j.commatsci.2022.111889.
- [69] W. Hanke and L. J. Sham, *Local-field and excitonic effects in the optical spectrum of a covalent crystal*, Phys. Rev. B **12**, 4501–4511 (1975), doi:10.1103/physrevb.12.4501.